Observations of Strong Surface Radar Ducts over the Persian Gulf

IAN M. BROOKS

Scripps Institution of Oceanography, La Jolla, California

ANDREAS K. GOROCH

Naval Research Laboratory, Monterey, California

DAVID P. ROGERS

Scripps Institution of Oceanography, La Jolla, California

(Manuscript received 15 May 1998, in final form 1 December 1998)

ABSTRACT

Ducting of microwave radiation is a common phenomenon over the oceans. The height and strength of the duct are controlling factors for radar propagation and must be determined accurately to assess propagation ranges. A surface evaporation duct commonly forms due to the large gradient in specific humidity just above the sea surface; a deeper surface-based or elevated duct frequently is associated with the sudden change in temperature and humidity across the boundary layer inversion.

In April 1996 the U.K. Meteorological Office C-130 Hercules research aircraft took part in the U.S. Navy Ship Antisubmarine Warfare Readiness/Effectiveness Measuring exercise (SHAREM-115) in the Persian Gulf by providing meteorological support and making measurements for the study of electromagnetic and electro-optical propagation. The boundary layer structure over the Gulf is influenced strongly by the surrounding desert landmass. Warm dry air flows from the desert over the cooler waters of the Gulf. Heat loss to the surface results in the formation of a stable internal boundary layer. The layer evolves continuously along wind, eventually forming a new marine atmospheric boundary layer. The stable stratification suppresses vertical mixing, trapping moisture within the layer and leading to an increase in refractive index and the formation of a strong boundary layer duct. A surface evaporation duct coexists with the boundary layer duct.

In this paper the authors present aircraft- and ship-based observations of both the surface evaporation and boundary layer ducts. A series of sawtooth aircraft profiles map the boundary layer structure and provide spatially distributed estimates of the duct depth. The boundary layer duct is found to have considerable spatial variability in both depth and strength, and to evolve along wind over distances significant to naval operations ($\sim$100 km). The depth of the evaporation duct is derived from a bulk parameterization based on Monin–Obukhov similarity theory using near-surface data taken by the C-130 during low-level (30 m) flight legs and by ship-based instrumentation. Good agreement is found between the two datasets. The estimated evaporation ducts are found to be generally uniform in depth; however, localized regions of greatly increased depth are observed on one day, and a marked change in boundary layer structure resulting in merging of the surface evaporation duct with the deeper boundary layer duct was observed on another. Both of these cases occurred within exceptionally shallow boundary layers ($\leq$100 m), where the mean evaporation duct depths were estimated to be between 12 and 17 m. On the remaining three days the boundary layer depth was between 200 and 300 m, and evaporation duct depths were estimated to be between 20 and 35 m, varying by just a few meters over ranges of up to 200 km.

The one-way radar propagation factor is modeled for a case with a pronounced change in duct depth. The case is modeled first with a series of measured profiles to define as accurately as possible the refractivity structure of the boundary layer, then with a single profile collocated with the radar antenna and assuming homogeneity. The results reveal large errors in the propagation factor when derived from a single profile.

1. Introduction

Anomalous radio propagation conditions—those differing from the propagation conditions for a ''standard'' atmosphere—are, the appellation not withstanding, very much the norm over the oceans. The various classes of anomalous propagation are summarized by Turton et al. (1988). The present study is concerned only with the class of anomalous propagation known as ducting in which radio waves become trapped within a shallow and near-horizontal layer. Under such conditions the propagation range can be greatly enhanced. The concentration of energy within the duct, however, results

Corresponding author address: Dr. Ian M. Brooks, Scripps Institution of Oceanography, UCSD, 9500 Gilman Dr., La Jolla, CA 92093-0230.
E-mail: brooks@myfanwy2.ucsd.edu

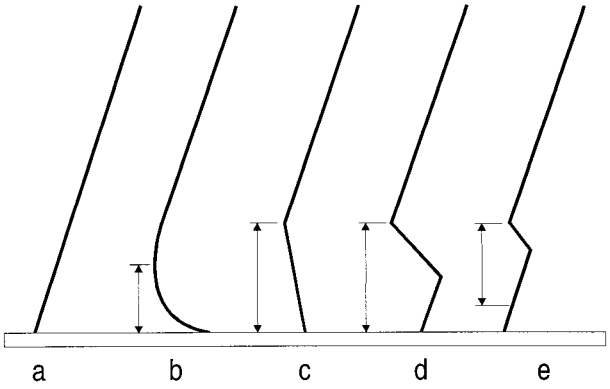

FIG. 1. Idealized *M* profiles for various types of radar duct: (a) standard atmosphere, no duct; (b) evaporation duct; (c),(d) surface ducts; and (e) elevated duct. The duct height *D* is indicated by arrows on each profile.

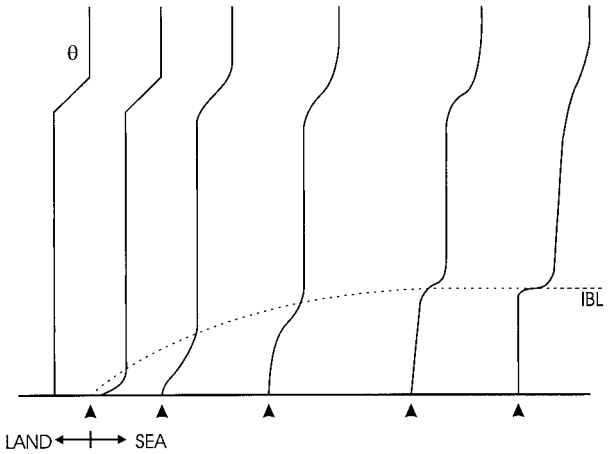

FIG. 2. Idealized representation of the alongwind evolution of the potential temperature profiles for an internal boundary layer. The initial profile is that just prior to advection over the coastline, and shows a deep, well-mixed boundary layer. As the distance from the shore increases, the IBL deepens and its potential temperature approaches that of the sea surface. The original BL inversion is slowly eroded. Ultimately a shallow, well-mixed marine layer may form. The dashed line represents the IBL depth; the arrows indicate the sea surface potential temperature.

in a corresponding reduction in the signal just above or below the ducting layer, and the formation of a radar ''hole'' where detection ranges are much reduced.

It is usual in studies of radar ducting to consider the modified refractive index *M*, defined by the empirical equation

$$M = \frac{77.6}{T}\left(P + \frac{4810e}{T}\right) + \frac{z}{10^{-6}r}, \qquad (1)$$

where *T* is atmospheric temperature in kelvins, *P* is total atmospheric pressure in millibars, *e* is water vapor pressure in millibars, *z* is height in meters, and *r* is the earth's radius in meters; *M* is dimensionless (Bean and Dutton 1968). The value *M* has the useful property that dM/dz is less than zero for ducting conditions, easily recognizable as an inversion in a vertical profile. Figure 1 shows idealized *M* profiles for the various types of duct: evaporation, surface-based, and elevated. The standard atmosphere profile (a) is obtained when all the parameters in Eq. (1) vary only with their standard atmospheric lapse rates. Evaporation ducts (b) result from the large humidity gradient commonly found just above the sea surface. They are typically of the order of a few meters to a few tens of meters deep, but vary with geographic location, season, and time of day. Surface-based [(c),(d)] and elevated (e) ducts may result from either large-scale subsidence or the modification of an air mass advected over a body of water. The large gradients in humidity and temperature across a subsidence inversion give rise to a trapping layer. Whether the duct reaches the surface depends upon the strength of the inversion and the depth and vertical structure of the boundary layer (BL) beneath it.

The BL is that part of the atmosphere that is influenced directly by the surface. In coastal regions an air mass advected from the land over the water may experience a large change in surface roughness, temperature, and humidity. The air closest to the surface adjusts rapidly to the change in surface conditions. Consider the advection of warm, dry, continental air over a cooler body of water. Heat loss to the surface results in the cooling of the air nearest the surface and the formation of a stable layer within the existing boundary layer—a stable internal boundary layer (IBL). An upward flux of moisture from the surface humidifies the near-surface air; the stability of the layer suppresses vertical mixing and thus traps moisture within the shallow IBL. The decrease in temperature and increase in humidity cause an increase in *M*. The gradients across the top of the stable layer result in a trapping layer and the formation of a duct. As the air mass moves downstream the internal boundary layer may continue to evolve for several hundred kilometers (Garratt 1990), deepening, moistening, and eventually reaching equilibrium with the surface. At the same time, the old BL that had existed over land, cut off from the surface by the stable layer below, is eroded slowly away. Ultimately, the internal boundary layer formed at the coast may become the only recognizable boundary layer and is considered the boundary layer proper, rather than a layer within a deeper BL. Figure 2 shows an idealized representation of internal boundary layer evolution. Early measurements of internal boundary layer development and their associated radio propagation conditions are presented by Craig (1946) and Emmons (1947). A more recent example of a strong surface-based duct formed by advection of warm, dry air over cooler water is given by Babin and Rowland (1992). A succession or combination of different processes may result in surface-based or elevated ducting layers coexisting with evaporation ducts, or for multiple ducts to coexist at different levels. Note that although there is no clear distinction between evapo-

ration and surface-based ducts, the former being a subset of the latter, they do present different measurement problems, as explained below. For the purposes of this paper we will consider them separately and define surface-based or boundary layer ducts to be those where the trapping layer corresponds with a well-defined boundary layer inversion, and evaporation ducts to be near-surface features associated with strong gradients in temperature and humidity within the lowest levels of the boundary layer.

Both surface evaporation and boundary layer ducts are common over the oceans (Craig 1946; Emmons 1947; Abdul-Jauwad et al. 1991; Babin 1996; Babin et al. 1997). Babin (1996) examined a total of 116 days of soundings made by an instrumented helicopter off Wallops Island, Virginia, during all seasons and a variety of meteorological conditions. Surface-based or evaporation ducts were present 74% of the time but no attempt was made to distinguish between them. Evaporation ducts below the 3-m minimum measurement level are not included in the Wallops Island dataset, implying an even higher frequency of occurrence.

The strength of a radar duct is quoted in terms of the maximum wavelength (or minimum frequency) trapped by the duct. For a simple surface-based or elevated duct this is given by the expression

$$\lambda_{\max} = \frac{2}{3} CD\Delta M^{1/2}, \tag{2}$$

where $\lambda_{\max}$ is the maximum trapped wavelength (m), D is the duct depth (m), ΔM is the difference between the minimum in M at the top of the duct and the maximum value within the duct (note that this is not necessarily the value of M at the bottom of the duct), and $C = 3.77 \times 10^{-3}$ for a surface-based duct, and $C = 5.66 \times 10^{-3}$ for an elevated duct (Turton et al. 1988). In reality the cutoff wavelength for a duct is not sharply defined and wavelengths longer than $\lambda_{\max}$ will be ducted to some extent; nor is the duct perfect for wavelengths shorter than $\lambda_{\max}$, and some energy will always leak out of the duct.

The effects of radar ducting are important for several reasons: ducting can modify the effective range of radio communications and navigation radar used by shipping, and its effects must be removed from weather radar returns before determining precipitation rates (Moszkowicz et al. 1994). It is of particular interest to naval operations, for which knowledge of surface duct height is of critical importance in predicting radar propagation and hence target detection ranges. Depending upon the relative heights of antenna, duct, and target, the duct may greatly enhance or reduce the detection range. Routine ship-based soundings may be sufficient to identify boundary layer ducts but evaporation ducts are more difficult to characterize since it is not usually feasible to make profile measurements within a few meters of the sea surface. Point measurements from a fixed height are used with a bulk parameterization to calculate the local depth of the evaporation duct. A number of such evaporation duct models are reviewed by Babin et al. (1997).

To assess the effect of measured or parameterized refractivity profiles a radar propagation model is used to calculate a propagation factor as a function of range and height. Typically only a single measured profile is available, often located at the radar source—a rawinsonde profile made from a ship, for example. The single profile is used as input to the model and the assumption is made that refractivity conditions are uniform over the range of the model, typically on the order of 50–100 km. In a heterogeneous environment the assumption of homogeneity may result in significant errors in the calculated propagation factor. A recent study by Goldhirsh and Dockery (1998) examined 30 cases where a series of spatially distributed refractivity profiles defined a two-dimensional cross section through the atmosphere. They modeled the radar propagation using first the full series of profiles then a single profile only, and determined the error resulting from the assumption of homogeneity. Their analysis treated the problem on a purely statistical basis and derived the probability of the error being greater than some value over a defined region of the model output field.

The measurements presented in this paper were made by the U.K. Meteorological Office's Meteorological Research Flight (MRF) C-130 Hercules aircraft over the Persian Gulf during late April 1996. Additional measurements were obtained from coastal weather stations, a U.S. Navy ship-based instrumentation package, and rawinsonde launches. The measurements were made in support of a U.S. Navy Ship Antisubmarine Warfare Readiness/Effectiveness Measuring exercise (SHAREM-115). One of the goals of such exercises is to evaluate the impact of environmental conditions on electromagnetic and electro-optical systems. The latest generation of weapon, sensor, and communication systems is more sensitive to environmental conditions than are the systems it replaces; it has thus become essential to consider not just the large-scale or mean environment, but also the effects of small-scale variability.

The Persian Gulf is entirely surrounded by desert landmass (Fig. 3). The BL above such an enclosed sea rarely will be free of the effects of the surrounding land since advective effects will influence the BL regardless of wind direction (Smedman et al. 1997). Hot, dry air coming off the desert over the Gulf rapidly will form a stable IBL and associated radar duct. Abdul-Jauwad et al. (1991) studied two years worth of 12-hourly soundings from a coastal station in Saudi Arabia and found a surface radar duct to exist most of the time, with a mean depth of 40 m.

We examine first the general boundary layer conditions prevailing during the observation period (section 3a). The boundary layer is the region of greatest interest for ship-based radar and it is important to relate radar

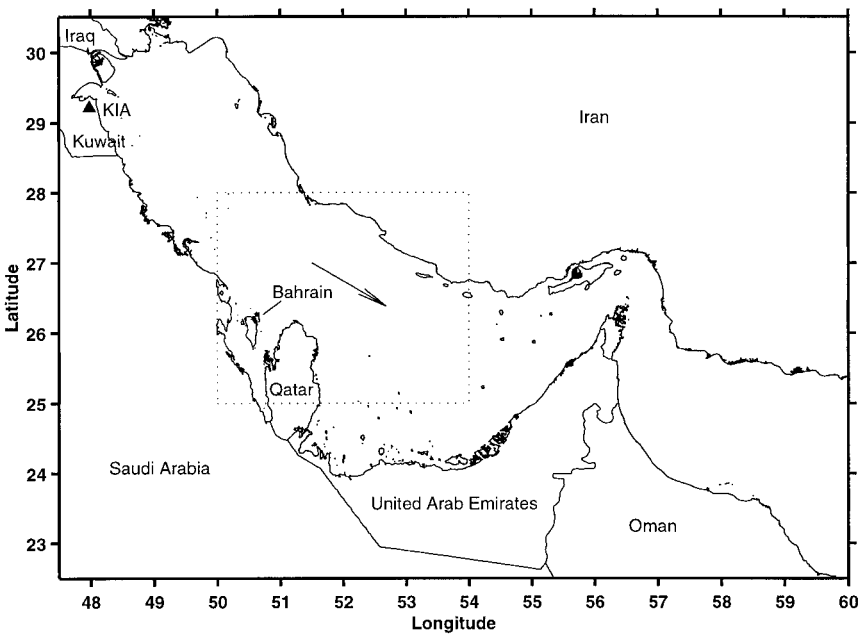

FIG. 3. Map of the Persian Gulf. Kuwait International Airport is marked by the solid triangle. The region marked by a dotted line around the central Gulf corresponds to the area shown in other maps throughout this paper. The arrow shows the mean boundary layer wind direction throughout the observing period.

propagation studies back to BL conditions and processes to understand how to apply the results more widely. Observations of BL and surface evaporation ducts are examined separately to assess their spatial variability (sections 3b and 3c). Last, we model radar propagation for one of the cases to illustrate the effect of spatial variability on the propagation factor and the errors arising from the use of a single profile and assumed homogeneity (section 4).

2. Measurements

The MRF C-130 Hercules is a well-instrumented atmospheric research aircraft. Its standard suite of instruments measures a wide range of meteorological, dynamic, radiative, and microphysical variables. Table 1 lists details of measurement accuracy and resolution for the primary variables used in this study. The three wind components are derived from a pitot–static pressure sys-

TABLE 1. Primary variables used in this study, the instrument types and manufacture, and measurement accuracy and resolution (combined performance of the instrument, signal conditioning, and logging system).

Variable	Instrument type	Manufacturer	Accuracy	Resolution
Aircraft measurements				
Air temperature	Platinum resistance	Rosemount 102BL	±0.3°C	0.006°C
Static pressure	Variable capacitance	Rosemount 1201F	±1 mb	0.25 mb
Surface temperature	Pyroelectric detector	Heimann	±0.5°C	0.1°C
Total water content	Lyman-α absorption hygrometer	U.K. Meteor. Office	±0.15 g kg^{-1}	0.005 g kg^{-1}
Dewpoint temperature	Thermoelectric hygrometer	General Eastern 1011B	±0.25°C (>0°C)	0.03°C
Wind speed	Gust vanes, Pitot–static system, inertial platform, GPS	Penny & Giles Rosemount 1221F Honeywell H423 NAVSTAR XR5	±0.4 m s^{-1}	0.06 m s^{-1}
Altitude	Radar altimeter	Honeywell	±1%	0.4 m
Ship-based measurements				
Air temperature	Platinum resistance	Rotronics MP-100	±0.3°C	0.1°C
Air pressure	Variable capacitance	Setra Model 720	±0.5 hPa	0.1 hPa
Surface temperature	Pyroelectric detector	Heimann KT-19	±0.5°C	0.1°C
Relative humidity	Capacitance	Rotronics MP-100	1%	1%
Wind speed	Propeller/vane	R. M. Young 04101	±0.5 m s^{-1}	0.1 m s^{-1}

TABLE 2. Flight times and some boundary layer properties for SHAREM-115. All values are means for 30-m flight legs except the maximum wind speed values, which were obtained just above the inversion.

Date/flight No.	Times (UTC)	Inversion height (m)	T (K)	SST (K)	Q (g kg^{-1})	WD (°)	WS (m s^{-1})	WS (max) (m s^{-1})
23 Apr/A451	0938–1652	~70	299.6	299.3	16.1	283	6.3	9
25 Apr/A452	0600–1150	~100	298.9	298.5	15.3	306	5.9	12
27 Apr/A453	0905–1300	200–300	297.9	297.9	11.4	310	14.3	23
28 Apr/A454	0305–1035	250–300	297.7	297.1	10.5	315	13.0	23
29 Apr/A455	0940–1620	250	298.7	297.8	11.0	301	13.4	22

tem and two wind vanes, or gust probes, all situated at the tip of a 7-m long nose boom in the relatively undistorted airflow ahead of the aircraft. Aircraft motions are monitored by an inertial navigation unit that is corrected for long-period drift and Schuler oscillations by comparison with a global positioning system (GPS). The temperature measurements used in this study are derived from a Rosemount platinum resistance thermometer situated 1–2 m behind the wind probes on the nose boom. Dewpoint temperature and total water mixing ratio are measured by a Lyman-α absorption hygrometer situated at the base of the nose boom. The Lyman-α suffers from a drift in the zero offset over the course of a flight that is corrected by continuous calibration against a General Eastern cooled-mirror hygrometer when in clear air. All five of the flights presented here were conducted entirely in clear air so that the Lyman-α calibration should not suffer any periods of degradation. The sea surface temperature (SST) is measured radiometrically by a Heimann infrared radiometer. The SST data are not corrected for nonunity emissivity of the surface. The resultant error is estimated to be on the order of -0.1 K. Aircraft altitude is determined by radar altimeter up to 1500 m; above this height the altitude is determined from the atmospheric pressure. Most parameters are sampled at 32 Hz; 1-s mean values are used throughout this analysis.

A total of five flights were made between 23 April and 29 April, based out of Bahrain. Flying times and locations were determined by the need to fit in with the operations of the naval exercise. Table 2 gives details of flight times and some relevant boundary layer parameters. The sampling strategy was designed to characterize the vertical structure and horizontal variability of the boundary layer. A typical flight consisted of stacks of straight and level flight legs and a series of sawtooth profiles from approximately 15 m to just above the inversion, over fixed ground tracks (Fig. 4). This flight pattern provided a dense set of measurements from which two-dimensional cross sections through the lower troposphere could be constructed to provide a clear visualization of the boundary layer structure. The cross sections were oriented both across and along the approximate wind direction—the precise orientation was

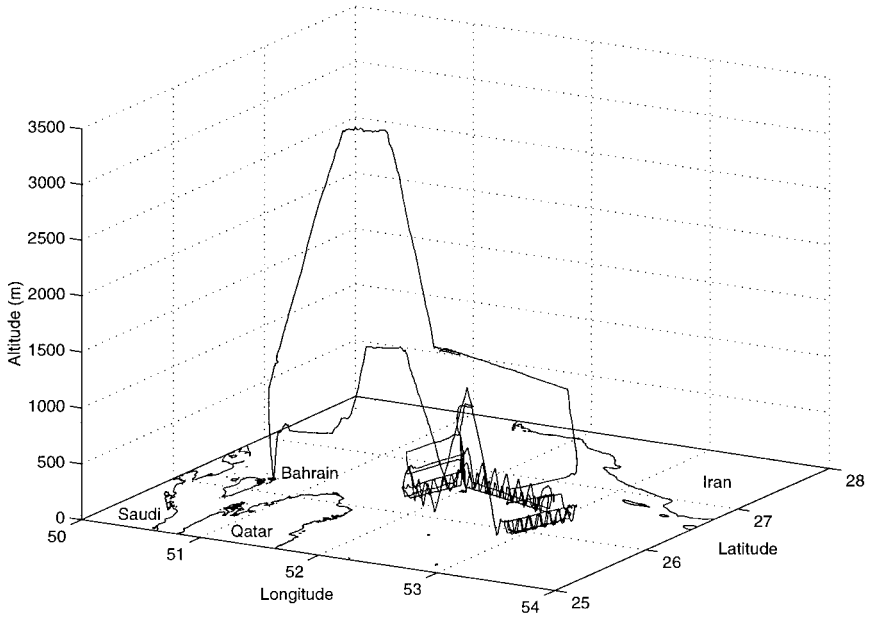

FIG. 4. The aircraft flight track on 25 Apr. Flight tracks on 23 and 28 Apr followed a pattern similar to that shown here; on 27 and 29 Apr, tracks were flown only along the Gulf, oriented NW–SE.

limited by the proximity of Iranian airspace to the northeast. Occasional deeper profiles were made from 15 m up to 1500 m.

Near-surface meteorological measurements were made from the USS *Caron.* Air temperature and relative humidity were measured by a Rotronics MP-100 probe, and wind speed and direction were measured by an R. M. Young wind vane. The instruments were located on the jack staff at the prow of the ship approximately 17 m above the waterline and 20 m from the main superstructure. Flow distortion is unavoidable on a large platform such as a ship but should be minimized by the instrument siting and is not expected to bias much our results. Sea surface temperature was measured by an infrared radiometer mounted on the stanchion on the foredeck at the bow and angled 30° from the vertical to keep the hull out of the field of view while minimizing cold sky reflection. No corrections were made to account for the nonunity emissivity of the sea surface, but periodic comparisons with direct measurements showed agreement to be within 0.2 K. One-min averages of the ship data are used in this analysis. Occasional rawinsonde soundings were also made from the *Caron.* Measurements of the initial boundary layer state at the coast prior to advection over the Persian Gulf are obtained from synoptic upper-air reports from Kuwait International Airport (KIA), several hundred kilometers to the northwest (see Fig. 3).

3. Observations

a. Meteorological conditions

Mean boundary layer conditions for the five research flights fall into two distinct groups and are summarized in Table 2. On 23 and 25 April, winds were light and variable, blowing from between west and northwest on the 23d with a maximum of 9 m s^{-1} just above the inversion and from between northwest and north with a maximum of 12 m s^{-1} on 25 April. The boundary layers were very shallow, between 70 and 100 m on both days. The remaining three flights took place during a period when the synoptic flow was dominated by a region of high pressure over Turkey with a secondary high over Saudi Arabia, resulting in a winter shamal. Such events are dominated by high northerly winds (*shamal* is an Arabic word meaning north), occur episodically from November through March, and are associated with midlatitude disturbances moving from west to east (Perrone 1979). The shamal was accompanied by wind speeds of up to 23 m s^{-1} just above the inversion, falling to around 12 m s^{-1} near the surface; mesoscale subsidence over the Gulf; and increased sea state. The wind direction was consistently from between northwest and north-northwest, more or less straight down the length of the Gulf. The longer overwater fetch and greater mixing from the high winds resulted in deeper boundary layers (200–300 m) than on the earlier flights.

While the wind speed and boundary layer depth vary considerably between the earlier and later flights, the general development of the boundary layers is very similar. Synoptic upper-air soundings at coastal stations upwind of the operational area show deep (1000–3000 m), well-mixed, convective boundary layers. The mean BL potential temperature was 3–6 K warmer than the Gulf surface water temperature. No observations are available immediately downwind of the coast, but the typical evolution of a warm air mass advected over a cooler body of water has been documented in a number of recent experimental studies (Garratt and Ryan 1989; Hsu 1983; Rogers et al. 1995; Smedman et al. 1997). Heat loss to the surface cools the lowest part of the BL, resulting in the formation of a shallow stable IBL. Wind shear increases across the stable layer and mechanically driven turbulence entrains air from above, slowly deepening the layer. The surface humidity flux rapidly moistens the layer, and the stability of the layer suppresses vertical transport, trapping moisture near the surface. By the time it is sampled by the aircraft, the IBL has evolved to the point where it can be considered a shallow marine atmospheric boundary layer proper, rather than an IBL within the remains of the overland convective boundary layer.

Figure 5 shows profiles of potential temperature, total water mixing ratio, and wind speed and direction on 28 April from the coastal synoptic reporting station at KIA near the northwestern end of the Persian Gulf and a rawinsonde ascent from the USS *Caron* at the southeastern end of the operational area. It is assumed that the sounding at KIA is representative of the air mass prior to advection over the Gulf waters; it shows a well-mixed convective boundary layer approximately 1800 m deep. The rawinsonde profile some 600 km downwind shows a much shallower, stable boundary layer, approximately 300 m deep. It has cooled considerably toward the sea surface temperature and the near-surface water vapor mixing ratio has increased by a factor of about 4. The original boundary layer is no longer distinct and the IBL formed at the coast, though still evolving, has become the new boundary layer. The general warming of the lower atmosphere is associated with the mesoscale subsidence that accompanied the shamal. It should be noted that, while these soundings illustrate the general evolution of the boundary layer, the airflow is not directly between the two, and air sampled by the rawinsonde would have crossed the coast earlier in the day than that sampled at KIA.

b. Boundary layer ducts

The change in general meteorological conditions during SHAREM-115 is reflected in the evolution of the boundary layer duct during the week. Figure 6 shows a time–height section of $\partial M/\partial z$ for the week during

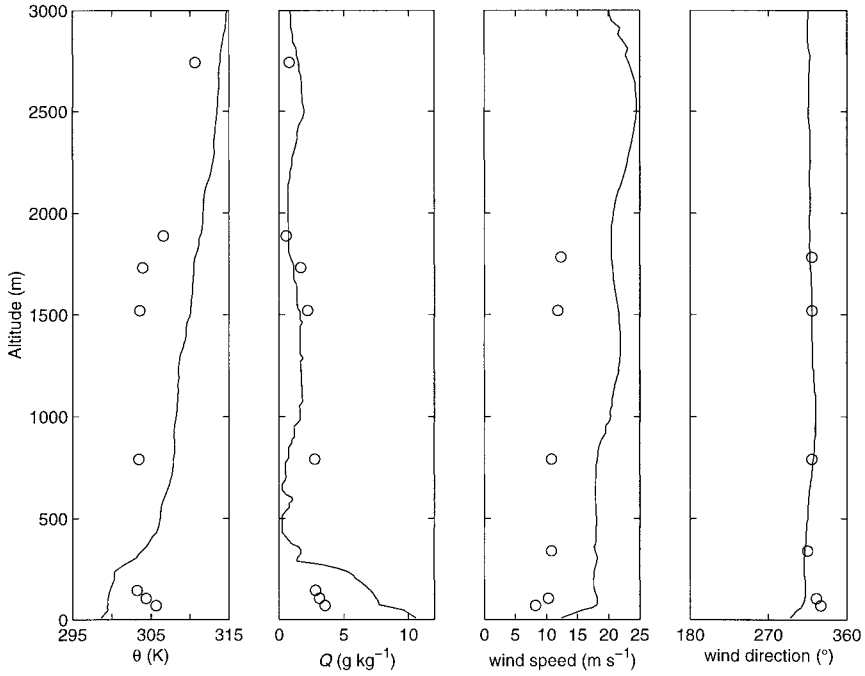

FIG. 5. Profiles of potential temperature (θ), total water mixing ratio (Q), wind speed, and wind direction from the coastal synoptic reporting station at Kuwait International Airport (29°13′N, 47°59′E) at 1200 UTC (○) and from a rawinsonde ascent from the USS *Caron* at 26°09′N, 53°06′E at 1330 UTC (——) on 28 Apr.

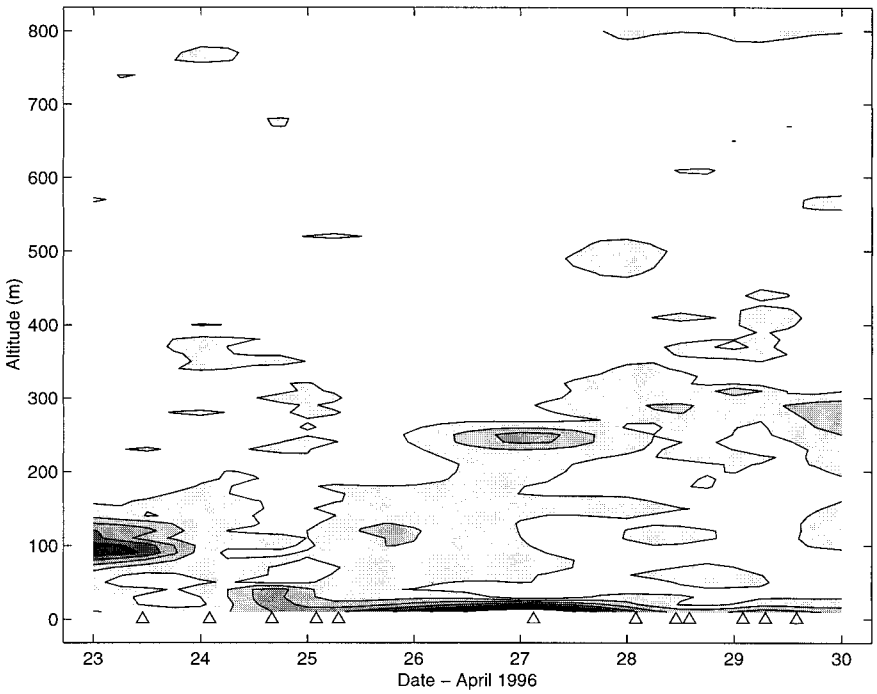

FIG. 6. Time–height section of $\partial M/\partial z$ generated from rawinsonde ascent profiles made from the USS *Caron* interpolated onto a 10 m × 6 h grid. A C-130 profile is included for 23 Apr since no rawinsonde ascent was made that day. The triangles at the surface indicate the time of each profile. Trapping layers ($\partial M/\partial z < 0$) are shaded and contoured at intervals of 0.5 M units m^{-1}. Tick marks are located at 0000 UTC on the date shown by the tick label.

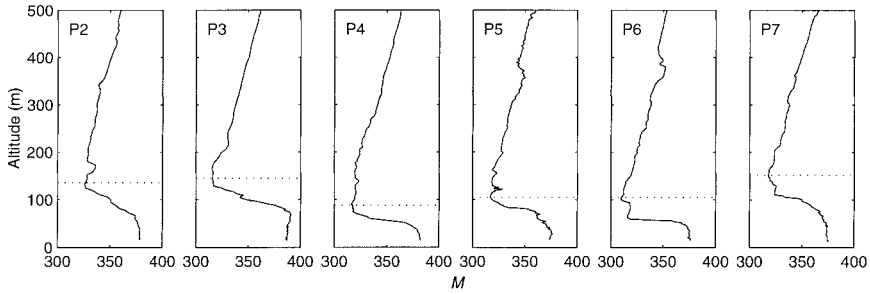

FIG. 7. Aircraft profiles of modified refractive index *M* from 23 Apr. The portion of each profile shown consists of approximately 2 min of data taken at the following times (UTC) and positions: P2, 1010, 26°38′N, 51°54′E; P3, 1124, 26°12′N, 53°07′E; P4, 1239, 25°49′N, 52°54′E; P5, 1255, 26°05′N, 52°02′E; P6, 1411, 26°07′N, 52°27′E; P7, 1413, 26°07′N, 52°27′E.

which aircraft observations were made, generated from rawinsonde ascents made from the USS *Caron* and one aircraft profile from 23 April since no rawinsonde ascents were made that day. There is a clear division between the shallow (≤150 m) ducting layer from 23 April through 25 April and the deeper (~300 m) duct on 28 and 29 April. The transition between the two regimes is not resolved because of the lack of soundings during a period of some 44 h between 25 and 27 April. Some of the structure visible during this period, while not physically unrealistic, is a result of the interpolation—a biharmonic spline (Sandwell 1987) that produces a smooth surface. Note that the rawinsonde soundings were made over a range of positions from 26° to 26°42′N and 52°12′ to 53°24′E though mostly at the southeastern end of this range and at varying times of day, with a bias toward early morning soundings. No attempt has been made to compensate for spatial or diurnal variability in the data contributing to the time–height section. The near-surface trapping layer visible below about 30–40 m on 23 April and 25–29 April is due to the surface evaporation duct and will be discussed in section 3c.

The large number of profiles made by the C-130 during SHAREM-115 provides a large dataset of spatially distributed estimates of duct height and strength. In excess of 200 profiles were made over the five flights, of which 169 provide usable profiles of modified refractive index. The remaining profiles do not resolve adequately the trapping layer because of an insufficient vertical range. Figures 7 and 8 show examples of aircraft profiles of *M* from 23 and 29 April, respectively. The duct heights are marked on each profile and show considerable variability. Note that the aircraft profiles are made at a very shallow angle of ≤3° to the horizontal and thus sample the horizontal variability as well as the vertical structure of the atmosphere. The large difference between typical atmospheric length scales in the horizontal and vertical allows the profiles to be treated as vertical for many applications, though care is needed where horizontal gradient or variability is large. For this reason we have neglected small-scale structure in the *M* profiles when selecting the top of the ducting layer. A high degree of variability is evident in both the duct depth and the overall structure of the refractivity profile. The latter reflects the poor and intermittent mixing often found in stable boundary layers (Nappo and Bach 1997). The profiles on 29 April (Fig. 8) show a greater degree of small-scale structure within the boundary layer. This structure is due to the increased mixing across the inversion in the higher winds, which brings warm, dry air into the boundary layer. Once the air is entrained, mixing within the strongly stable upper boundary layer is relatively poor and on a small scale, leading to highly variable air properties. Boundary layer duct depth statistics are given in Table 3.

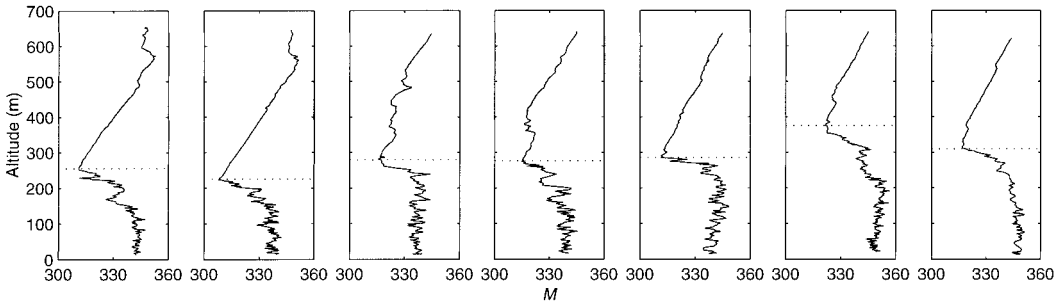

FIG. 8. Aircraft profiles of modified refractive index *M* from 29 Apr. These profiles form a sawtooth run downwind along the length of the area of operations from 26°38′N, 51°43′E to 26°04′N, 53°40′E and between the times of 1002:40 and 1032:50 UTC.

TABLE 3. Boundary layer duct depth statistics (m). Dates are for Apr 1996.

Date	No. of data points	Mean	Min	Max	Std dev
23	6	121.8	87.7	152.0	25.8
25	58	118.1	60.5	221.9	41.2
27	29	250.5	206.1	333.3	30.8
28	38	323.8	225.1	419.6	47.9
29	38	285.7	198.5	376.6	31.9

Duct height and ΔM have been evaluated and the consequent duct strength λ_{max} has been calculated for each of the aircraft profiles. The quantities ΔM and λ_{max} are plotted against duct depth in Figs. 9 and 10, respectively. The individual values of ΔM and λ_{max} cluster around different means on each day, reflecting the changes in mean boundary layer conditions. Considerable variability about these means is evident. Duct depth varies by a factor of up to 4, while ΔM varies by approximately ± 10 to ± 15 about the mean value on any given day. Here, ΔM is not correlated with the duct depth since it depends primarily on the changes in temperature and humidity across the inversion; these are largely unaffected by local changes in the inversion height. Duct strength λ_{max} is derived from the duct depth and ΔM [Eq. (2)]. The linear dependence on duct depth is obvious in Fig. 10. The remaining variability for a given duct depth is due to variations in ΔM.

Figures 11–13 show D, ΔM, and λ_{max} plotted against longitude, which is used as a surrogate for distance along wind. A linear or second-order polynomial least squares fit is shown for each case to emphasize the general alongwind trend. Duct height depends strongly on boundary layer depth and does not display a consistent trend along wind across all five days (Fig. 11). On 23 April there is no significant trend, though the small number of data points available means this is a tentative assessment. On 25 April there is an initial sharp increase and then a more gentle decrease in duct height; this behavior follows closely the general change in boundary layer depth observed during the alongwind flight legs on this day (not shown) and associated with changes in mixing across the inversion. On 27 April there is a slight decrease and then an increase in duct height. A linear fit to these data shows no significant trend along wind. On 28 April there is a clear decrease in duct height along wind following a steady decrease

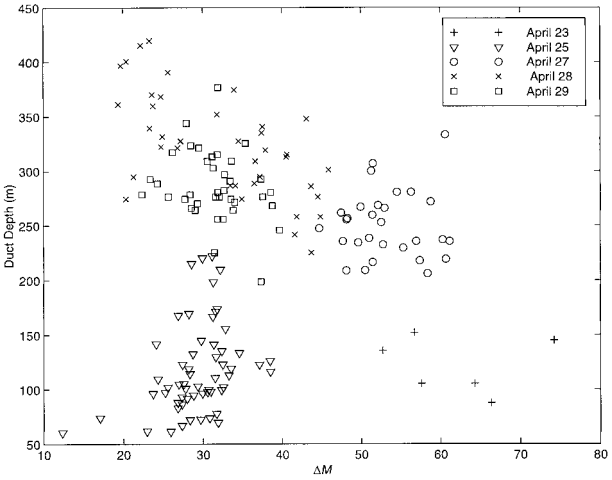

FIG. 9. Scatterplot of ΔM and duct depth D for 169 profiles taken from all five flights.

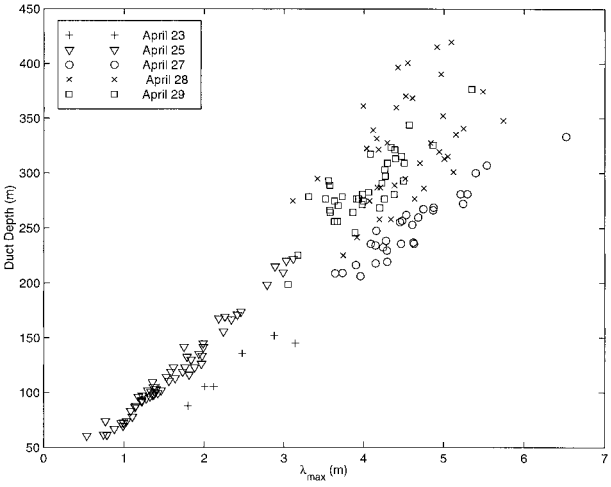

FIG. 10. As Fig. 9 but for λ_{max} and D.

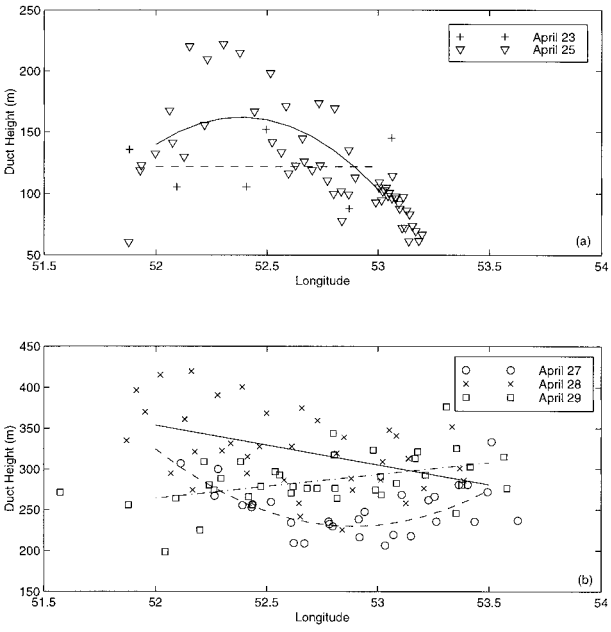

FIG. 11. Variation of duct depth D with longitude (proportional to distance along wind) for (a) 23 Apr (+, dashed line) and 25 Apr (▽, solid line); and (b) 27 Apr (○, dashed line), 28 Apr (×, solid line), and 29 Apr (□, dot-dashed line). Note that the fitted lines are intended only as an indication of the general trend along wind. Wind direction is from left to right across the figure.

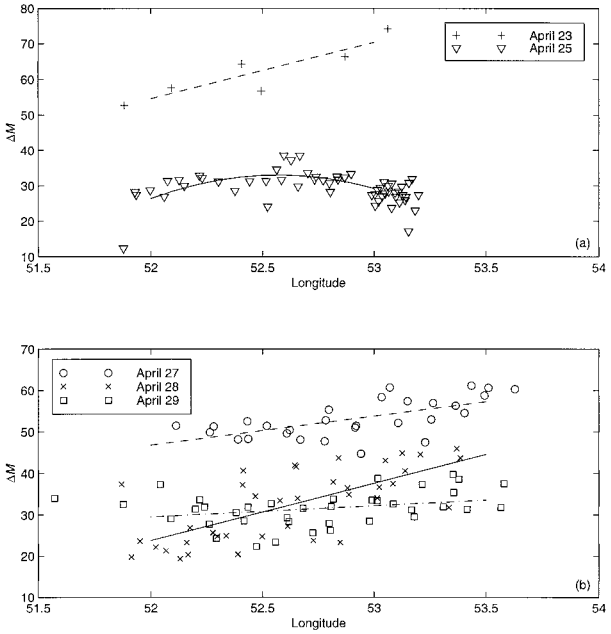

FIG. 12. As Fig. 11 but for ΔM with longitude.

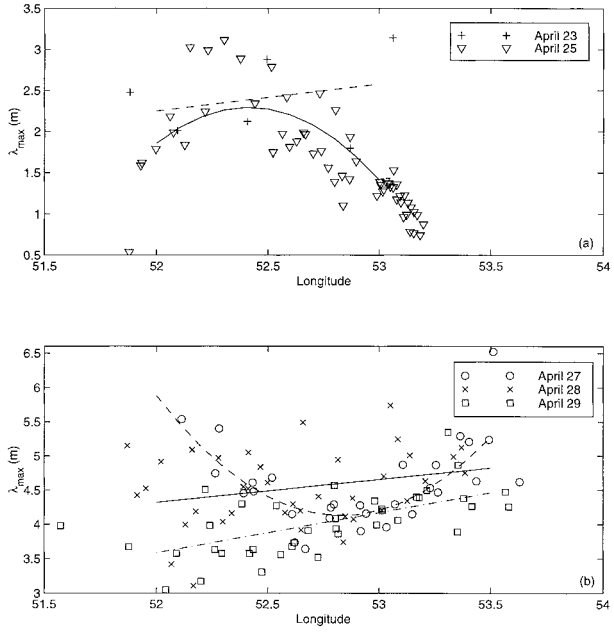

FIG. 13. As Fig. 11 but for maximum ducted wavelength λ_{max} with longitude.

in boundary layer depth associated with mesoscale subsidence over the Gulf. On 29 April the trend is a steady increase in duct depth. The different trends in duct depth observed during the shamal reflect changes in the relative rate of increase in BL depth caused by entrainment and depression of the inversion height due to subsidence.

The quantity ΔM (Fig. 12) shows a clear increasing trend along wind for all cases except 25 April. This trend is caused primarily by the increasing humidity of the boundary layer along wind, which itself results from the strong surface moisture fluxes and the strongly stable inversion that caps the boundary layer and inhibits transport out of the layer. The increasing humidity results in an increase in the refractive index within the BL and, hence, in the jump ΔM across the inversion. Figure 14 illustrates the changes in humidity and refractive index with profiles of total water mixing ratio and M at the upwind and downwind ends of the area of operations on 23 April. The increase in mixing ratio from ~17.1 to ~18.4 g kg^{-1} within the boundary layer and the consequent increase in M and strengthening of the radar duct are obvious. The day 25 April differs from the other cases: ΔM initially increases along wind as expected but then decreases again. This behavior is caused by the onset of strong mixing that brings drier air down across the inversion in the southeastern part of the measurement region, resulting in a net decrease in BL humidity. This process will be discussed in more detail in the next section.

The trend in λ_{max} (Fig. 13) is a result of the combination of the trends in D and ΔM, though dominated by the stronger dependence of λ_{max} on D. On 23, 28, and 29 April there is a steady increase in λ_{max} along wind; 27 April shows a minimum near the middle of the region; and 25 April is controlled by the duct depth, increasing then decreasing along wind.

c. Evaporation ducts

Evaporation ducts result from the large humidity gradient commonly found just above a water surface. They

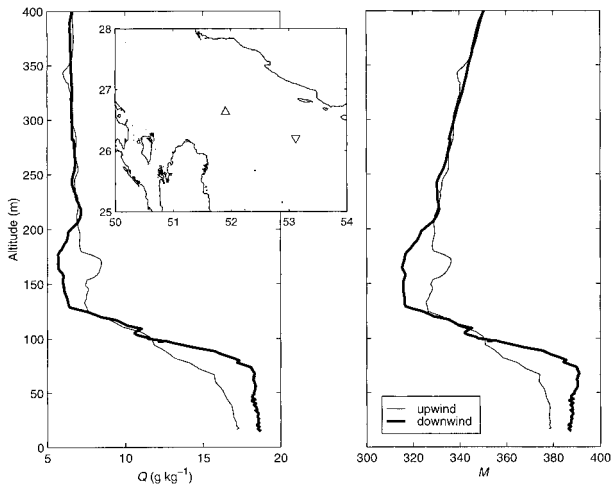

FIG. 14. Profiles of total water mixing ratio Q and modified refractive index M from 26°38′N, 51°54′E at 1010 UTC (upwind, thin line) and 26°12′N, 53°07′E at 1124 UTC (downwind, thick line) on 23 Apr. The increase in boundary layer humidity from ~17.1 to ~18.4 g kg^{-1} along wind, the consequent increase in M within the boundary layer from 377 to 389, and the strengthening of the radar duct are very clear. Inset is a map showing the locations of the upwind (△) and downwind (▽) profiles.

are present almost always over the oceans (Babin et al. 1997) and are typically a few meters to a few tens of meters deep. To assess accurately the propagation range for a ship-mounted radar antenna, typically located 20–30 m or so above the surface, the evaporation duct depth must be determined to an accuracy of 2 m or less (Babin et al. 1997). Direct measurement of the M profile within the lowest 10 meters or so of the BL over water is exceptionally difficult, and is not possible on a routine basis. Estimates of the depth of the evaporation duct thus usually are derived from measurements at a single height above the surface and a bulk parameterization. The parameterizations have their basis in Monin–Obukhov surface layer similarity theory, but until recently have relied heavily on empirical relationships to increase the computation speed rather than solving the similarity equations directly. The availability of powerful, cheap computers now permits the use of more complex parameterizations that incorporate explicit boundary layer physics (Babin et al. 1997). A recent comparison of such a parameterization, based closely on the Tropical Ocean Global Atmosphere Coupled Ocean–Atmosphere Response Experiment (TOGA COARE) bulk flux algorithm (Fairall et al. 1996), with a number of existing evaporation duct models and with direct observations found it to perform significantly better than the other models (Babin et al. 1997).

Evaporation duct depths have been estimated for the five flight periods during SHAREM-115 from both the C-130 data taken during the lowest level (30 m) flight legs and from data recorded by the deck-mounted instrumentation on the USS *Caron.* Near-surface profiles of temperature and humidity were derived from the TOGA COARE bulk flux algorithm and used to calculate profiles of M via Eq. (1). The parameterization has its basis in Monin–Obukhov surface layer similarity theory. The surface layer is defined to be that layer closest to the surface in which the fluxes can be considered to be constant with height. In practice, the layer in which fluxes vary by less than 10% of their surface values is acceptable; this layer corresponds approximately to the lowest 10% of the BL depth (Stull 1988). Within the surface layer, profiles of wind speed, temperature, and humidity are self similar; that is, when properly normalized by functions of surface parameters, the profiles collapse to form a set of curves that have the same shape. Given measurements at a known height and the surface temperature (wind speed is zero by definition at the surface, and humidity is assumed to be equal to the saturation value over water), the values at any height within the surface layer can be derived from the normalized profiles. A detailed description of the TOGA COARE bulk flux algorithm is beyond the scope of this paper; interested readers are referred to Fairall et al. (1996) for a thorough discussion of its background and workings.

Once a near-surface profile of M is derived, the evaporation duct depth is found by determining the level at which the gradient changes from negative to positive. A vertical interval of 0.2 m is used, starting at 0.2 m above the surface. Unfortunately, direct measurements of the structure of the duct for comparison with the bulk estimates are not available for SHAREM-115. The time section of $\partial M/\partial z$ in Fig. 6 indicates the evaporation duct trapping layer to be below about 30–40 m, but the resolution of the rawinsonde profiles is too coarse to characterize the structure and depth of the duct reliably. Although during profiles on 27–29 April the aircraft regularly descended below the top of the evaporation duct as estimated from the bulk parameterization, the shallow angle of the aircraft profiles coupled with the small gradient in M in the upper part of the evaporation duct means that the vertical structure is masked by the horizontal variability and the duct is not evident in any of the aircraft profiles.

Table 4 shows statistics for the estimates of evaporation duct depth from both the ship and aircraft. The ship estimates use 1-min averages for the period during which the C-130 was making measurements. The aircraft estimates are based on 1-s averages for the lowest-level (30 m) flight legs. Run numbers refer to individual flight legs as recorded in the MRF flight logs and are used here for ease of reference. The ship was located slightly to the north of the C-130 operating area on 23 April, within the flight area on 27 April, and to the southeast on 25 and 28 April. No ship data are available for 29 April. Wind measurements are not available from the ship for 23 and 25 April. Constant values of 6.0 and 5.6 m s^{-1} have been used for 23 and 25 April, respectively. These values are based on measurements from the C-130 reduced to the 17-m instrument height via the bulk flux algorithm. It is estimated from sensitivity tests that a 10% change in wind speed typically may result in up to $\pm 5\%$–10% change in the estimated evaporation duct height. The differences between the spatial distribution and location of the measurements mean that the duct height estimates from ship and aircraft are not directly comparable; however, close agreement is obtained for most cases.

We have noted that the bulk parameterization strictly is valid only within the surface layer, or lowest 10% of the BL. In this study the boundary layer is very shallow and on 27, 28, and 29 April the lowest-level flight legs at 30 m are very close to the top of the nominal surface layer. On 23 and 25 April they are well above the nominal surface layer, and even the ship-based measurements at 17 m are just above its upper limit. The estimates of evaporation duct depth, particularly those from the C-130, must thus be treated with some caution. First we will assume that the ship-based estimates are reliable. Comparison of them with the aircraft estimates shows good agreement on 23, 27, and 28 April and gives some confidence to the aircraft estimates, even when they are based on data taken above the nominal surface layer. On 25 April there is an exceptional case that displays large differences in estimated duct depth between

TABLE 4. Statistics for evaporation duct depth derived from bulk parameterization for both the USS *Caron* and the C-130. Dates are for Apr 1996. The ship-based values are derived from 1-min averages of measured quantities, the aircraft use 1-s averaged data. Run numbers refer to individual flight legs as recorded in the MRF flight logs and are used here for ease of reference. All duct heights are in meters, times in UTC.

Date	Time	Mean	Min	Max	Std dev
Ship					
23	1100:00–1640:00	12.4	6.8	26.2	3.0
25	0730:00–1130:00	—	—	—	—
27	0900:00–1230:00	20.7	17.6	34.4	1.8
28	0300:00–1000:00	20.6	17.4	28.8	1.8
Aircraft					
23, run 2	1130:38–1136:59	13.1	10.2	19.2	1.7
23, run 9	1257:13–1304:25	16.9	12.2	31.4	3.4
23, run 19	1450:01–1455:28	12.7	8.0	35.6	4.4
25, run 8	0744:53–0751:31	—	—	—	—
25, run 12	0838:22–0845:43	9.7	7.8	13.6	1.2
25, run 19 (a)	0951:31–0957:39	11.3	9.6	14.8	0.8
25, run 19 (b)	0957:40–1006:14	18.2	13.0	35.2	4.0
27, run 2	0956:34–1020:17	21.4	18.0	24.6	1.1
28, run 2	0355:50–0402:36	22.9	19.6	26.8	1.3
28, run 11	0537:02–0543:32	24.7	22.6	27.6	1.0
28, run 18	0651:41–0715:46	23.7	19.2	28.4	1.6
29, run 2	1035:35–1106:44	25.6	20.2	30.0	1.7
29, run 7	1315:48–1338:32	27.1	23.4	34.2	1.6

the upwind and downwind ends of the area of operations. The aircraft estimate from run 12 at the upwind end of the region indicates a relatively uniform, shallow evaporation duct. The upwind half of run 19, running along wind, shows similar values. The downwind half of run 19, however, shows a deeper duct with much greater variability; mean duct depth and variability both increase along wind (Fig. 15). Farther downwind at run

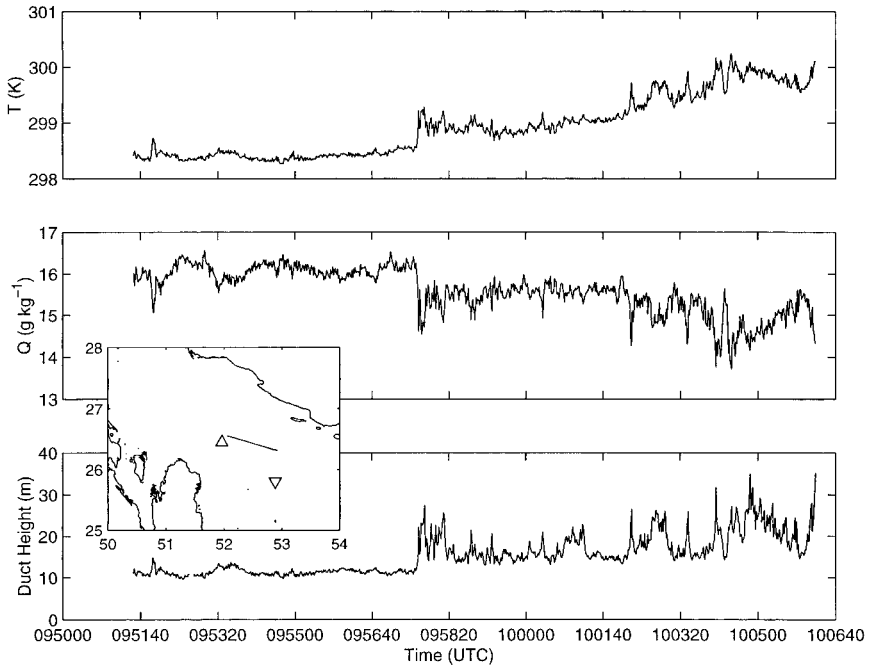

FIG. 15. Time series of temperature (T), total water mixing ratio (Q), and bulk duct depth for run 19 at 30 m on 25 Apr, running along wind from northwest to southeast (26°33′N, 52°03′E–26°18′N, 52°55′E). Note the sudden transition between a region of uniform estimated evaporation duct depth and a region with a deeper, much more variable duct. Inset is a map showing the locations of the flight track and of the upwind (△) and downwind (▽) profiles shown in Fig. 16 (note that the downwind profile is not collocated with the end of the alongwind run but is representative of the mean change in BL structure alongwind).

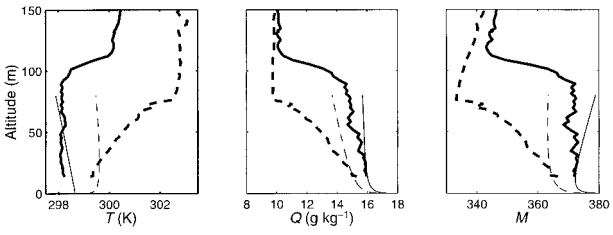

FIG. 16. Measurements of temperature (T), total water mixing ratio (Q), and modified radar refractive index (M) on 25 Apr from the aircraft profiles at the upwind (thick solid line: 1122 UTC at 26°27′N, 51°58′E) and downwind (thick dashed line, 0815 UTC, at 25°48′N, 52°53′E) ends of the measurement region. The thin lines show the associated bulk profiles based on data from 30-m runs close to the profile locations. Note that the bulk profiles have been extended above the level of validity for the parameterization in order to show clearly the altitude to which the assumed profile shape matches the actual profiles and to emphasize the difference above that level. The locations of the profiles are shown on the inset map in Fig. 15.

8 the parameterization no longer finds a top to the evaporation duct that is within the lower boundary layer. If the vertical range of the parameterization is extended upward sufficiently—well beyond its range of validity—values between 36 and 110 m are found. Note that the maximum value is above the boundary layer top, emphasizing the danger of accepting bulk estimates of the evaporation duct depth that are based on near-surface data without considering the boundary layer structure as a whole. The ship-based estimates are farther downwind still, and similarly fail to find a top to the evaporation duct that is within the lower boundary layer. Figure 16 shows measured aircraft profiles of temperature, humidity, and M at the upwind and downwind ends of the measurement region, along with bulk profiles of the same parameters based on data from 30-m flight legs close to the profile locations. The bulk profiles have been extended above the level for which the parameterization is valid so as to show clearly the altitude to which the assumed profile shape matches the observed profile and to emphasize the difference above that level. Note that the profile shape is more important than the absolute value since it is the gradient in M that defines the ducting region. Since the measured profile and the inputs to the bulk parameterization are separated spatially by about a kilometer or so and by up to 1.5 h, a perfect match is not expected; nevertheless the agreement is close, giving confidence in the parameterized profiles. The upwind measured and bulk profiles agree closely up to at least the level of the 30-m run, and the M profile clearly shows the shallow evaporation duct within the deeper boundary layer duct. The downwind profiles diverge from the measured profiles at a lower altitude, and it is clear that there is no distinct evaporation duct but rather it merges with the boundary layer duct. This conclusion is supported by comparison with Fig. 6. The trapping layer, as derived from rawinsonde ascents, is seen to be continuous from the surface to the inversion throughout most of 25 April.

The transition from the upwind region with a uniform duct to the deeper, highly variable duct is very rapid. The time series of temperature, humidity, and estimated duct depth in Fig. 15 show the transition to take place within a few seconds—a distance of a few hundred meters. The increase in temperature, decrease in humidity, and increase in variability of all parameters indicate an increase in the downwind mixing of warm, dry air across the inversion. This increase is confirmed by an increase in the vertical velocity variance. The cause of the mixing appears to be the breakdown of Kelvin–Helmholtz waves at the inversion, driven by a large shear across the inversion associated with a wind speed maximum just above the BL. No change in surface forcing, which might provide an alternative mechanism, is observed. The increased entrainment leads to the much more rounded shape of the humidity profile downwind compared with that upwind, as shown in Fig. 16. The much drier air mixed into the BL is sufficient to result in a net decrease in humidity along wind that causes the decrease in ΔM along wind observed for the boundary layer duct described in the previous section. The mixing is accompanied by a reduction in inversion height; this reduction accounts for the change from increasing to decreasing BL and BL duct depth along wind.

The duct depth statistics given in Table 4 show that the evaporation duct is relatively uniform over large areas for most of the observing period. In contrast to the BL ducts, no general trends in estimated evaporation duct depth or strength are observed with distance along wind. The estimated evaporation duct depth varies by just a few meters on 27, 28, and 29 April over distances of up to 200 km. Similarly the northwest part of the measurement area on 25 April shows very little variability. On 23 April, however, a great deal more variability is seen. Figure 17 shows time series of duct depth and air and sea surface temperature for one of the 30-m aircraft flight legs. The majority of the duct is relatively uniform in depth; however, two major regions are evident in which the duct depth doubles from about 15–30 m. Each region is about 5 km across, and displays large changes in duct depth within the space of a few hundred meters. Three smaller regions with a lesser increase in duct depth occur later in the time series. All of the regions of increased duct depth are associated with regions of decreased sea–air temperature difference. The increased stability in these regions results in subtle changes to the shapes of the temperature and humidity profiles and consequently to that of the M profiles, which change increases the level of the duct top.

4. Modeled radar propagation

The preceding sections have examined the spatial variability of the boundary layer and evaporation ducts observed over the Persian Gulf. To assess the significance of the variations in refractivity structure we must

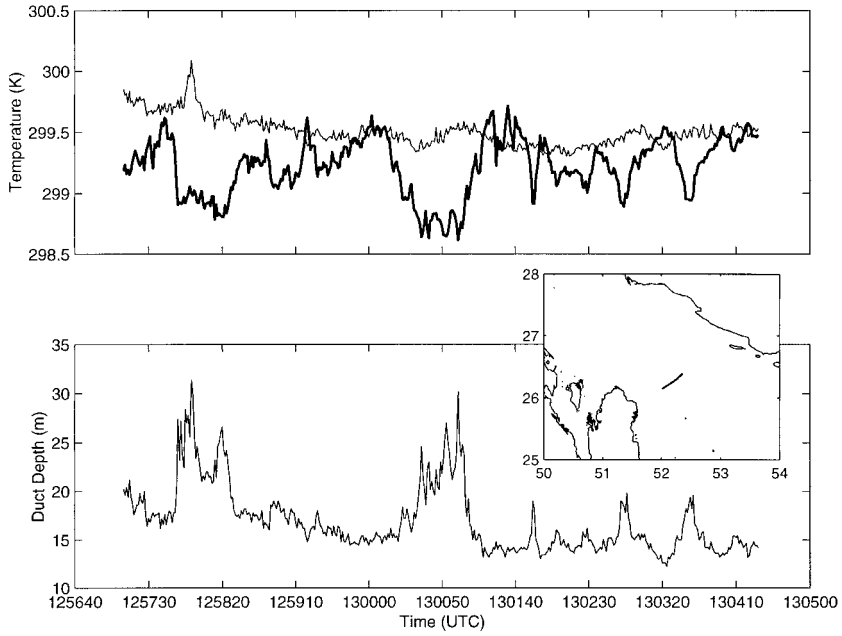

FIG. 17. Time series of air temperature (at 30 m) (thin line), sea surface temperature (thick line), and estimated evaporation duct depth for run 19 on 23 Apr (26°09′N, 52°01′E–26°23′N, 52°21′E). The duct is relatively uniform in depth with deeper regions where the sea surface temperature falls below the air temperature. The flight track is shown on the inset map.

model the resulting radar propagation field. We consider the case of alongwind variability on 25 April. This case is chosen since a dense series of 14 profiles were available that span a transition in the boundary layer and duct structure (Figs. 15 and 16). The profiles were made from approximately 15 m to just above the inversion (150–200 m) and spanned a range of 116 km with a mean separation of just under 9 km. The profiles were extended down to the surface using the bulk parameterization and up to 1000 m by matching the top of each profile with a single deep profile made at the upwind end of the region. Last, the profiles were smoothed and interpolated onto regular 1-m intervals for inclusion in the propagation model. Figure 18 shows a contoured cross section of the trapping layers ($\partial M/\partial z < 0$) derived from the profiles. At the upwind end of the region the BL duct is approximately 200 m deep, and the trapping layer extends throughout most of the BL depth. A shallow ($\sim$10 m) evaporation duct exists at the surface. The BL duct height and trapping layer depth decrease with distance downwind. The estimated evaporation duct depth increases beginning about 70 km downwind and then merges with the BL ducting layer to form a single trapping layer that extends through the entire BL depth.

We model the one-way radar propagation using the Tropospheric Electromagnetic Parabolic Equation Routine (TEMPER3) model. See Dockery (1988) for a discussion of propagation modeling with the parabolic equation. The radar modeled is an X-band radar operating at 10 GHz with the transmitter located 30 m above the surface, corresponding to the approximate characteristics of a ship-mounted search radar. Tests for lower frequencies produced similar results and are not presented here. Four cases are modeled. The first two cases use the full set of 14 profiles to define the refractivity structure and model the propagation along the section for transmitters located at the upwind (northwest) end of the region (Fig. 19a) and at the downwind (southeast) end of the section (Fig. 19b). The second two cases use the same transmitter locations but assume that the refractivity structure is homogeneous and defined by single profiles collocated with the transmitters (Figs. 19c,d). All four cases use a horizontal domain bounded by the positions of the first and last measured profiles.

The propagation conditions are dominated by the strong boundary layer duct with relatively little influence from the surface evaporation duct evident in the model output fields. Some major differences between the single-profile set and full-profile set cases immediately are obvious from the figures. The differences are isolated in Figs. 19e and 19f; these show the ''error'' fields that result from subtracting the single-profile fields from the corresponding ''true'' fields calculated from the full set of profiles. Regions colored yellow and red indicate underprediction of the propagation factor by the single-profile calculation; regions colored blue indicate overprediction. Close to the antenna ($<$30 km) there is very little error, as might be expected. At greater ranges, however, both the upwind and downwind cases show large contiguous regions of substantial error. Goldhirsh and Dockery (1998, referred to as GD98 hereinafter) suggest that 5 dB is an appropriate baseline error

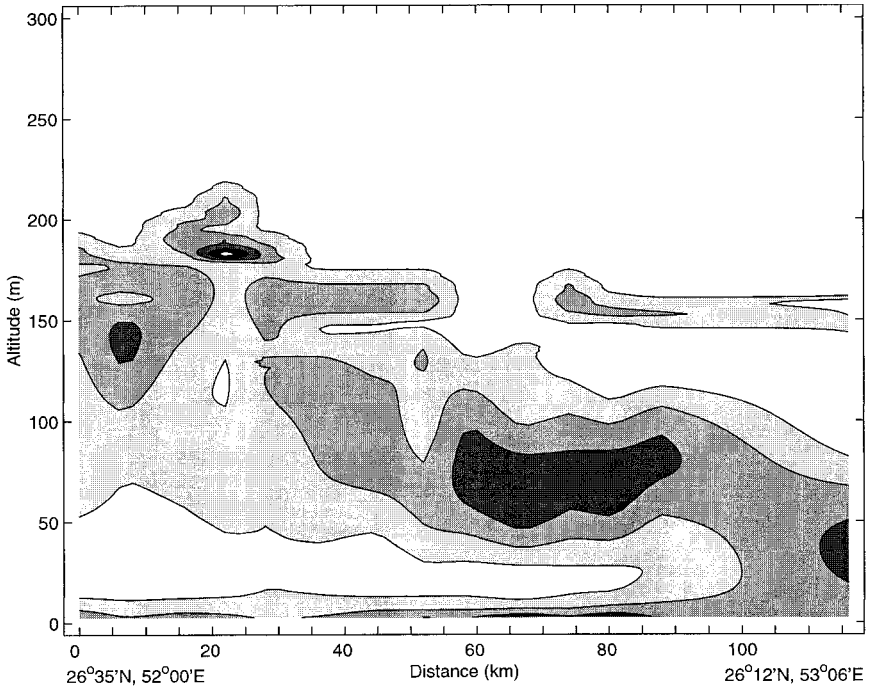

FIG. 18. Alongwind cross section of $\partial M/\partial z$ on 25 Apr running between 26°35′N, 52°00′E and 26°12′N, 53°06′E. Trapping layers ($\partial M/\partial z < 0$) are shaded and contoured at intervals of 0.25 M units m^{-1}.

for comparison of propagation factors. Their statistical study includes two scenarios comparable to those presented here, comparing propagation fields based on a single profile collocated with the antenna with those based on a spatially distributed set of seven profiles (GD98 Figs. 2 and 5). The GD98 study calculates the probability of the error exceeding some value as the fractional area of the propagation error field greater than that value. Their results are averaged additionally over a total of 30 cases selected without regard to the refractivity conditions. For a 10-GHz signal, GD98 indicate approximately 40% probability of the propagation error exceeding 5 dB within the range 30–90 km and altitude 5–300 m. Calculated over the same region, the present data show 49% and 57% of the error greater than 5 dB for the upwind and downwind cases, respectively. At greater ranges (90–115 km) the fractional areas increase further to 74% and 72%.

5. Summary and conclusions

Radar ducts are a common phenomenon over the oceans. A shallow evaporation duct forms in the strong humidity gradient just above the surface, and a boundary layer duct may form beneath the inversion that caps the marine atmospheric boundary layer. The effect of the ducts upon radar propagation is important for many applications and is critical to the use of naval radar detection systems, which typically are situated within or just above the surface evaporation duct.

The observations made by the U.K. Meteorological Office's C-130 research aircraft during the SHAREM-115 exercise in the Persian Gulf have provided an extensive set of spatially distributed measurements of both the boundary layer and surface evaporation ducts within a shallow marine boundary layer. During the weeklong observation period, the prevailing northwesterly winds brought warm, dry air from the desert over the cooler waters of the Gulf. The loss of heat to the surface results in the formation of a stable IBL that evolves continuously along wind. The C-130 sampled the air mass several hundred kilometers downwind from the coast, by which time little trace remained of the original deep convective boundary layer, and the IBL had effectively formed a new shallow marine boundary layer.

The initially relatively dry air moistened rapidly over the water, leading to an increase in the refractive index. The stable stratification suppressed vertical mixing, trapping moisture within the shallow boundary layer and resulting in a large humidity gradient across the inversion. This process was the major factor contributing to the formation of a strong boundary layer radar duct. The boundary layer duct followed the topography of the inversion layer. This behavior may be affected by a number of factors: synoptic and mesoscale processes such as subsidence; topographic forcing of the mean flow; changes to surface forcing; shear-induced mixing at the inversion; and, in stable conditions as here, by gravity waves. Considerable variability in boundary layer duct

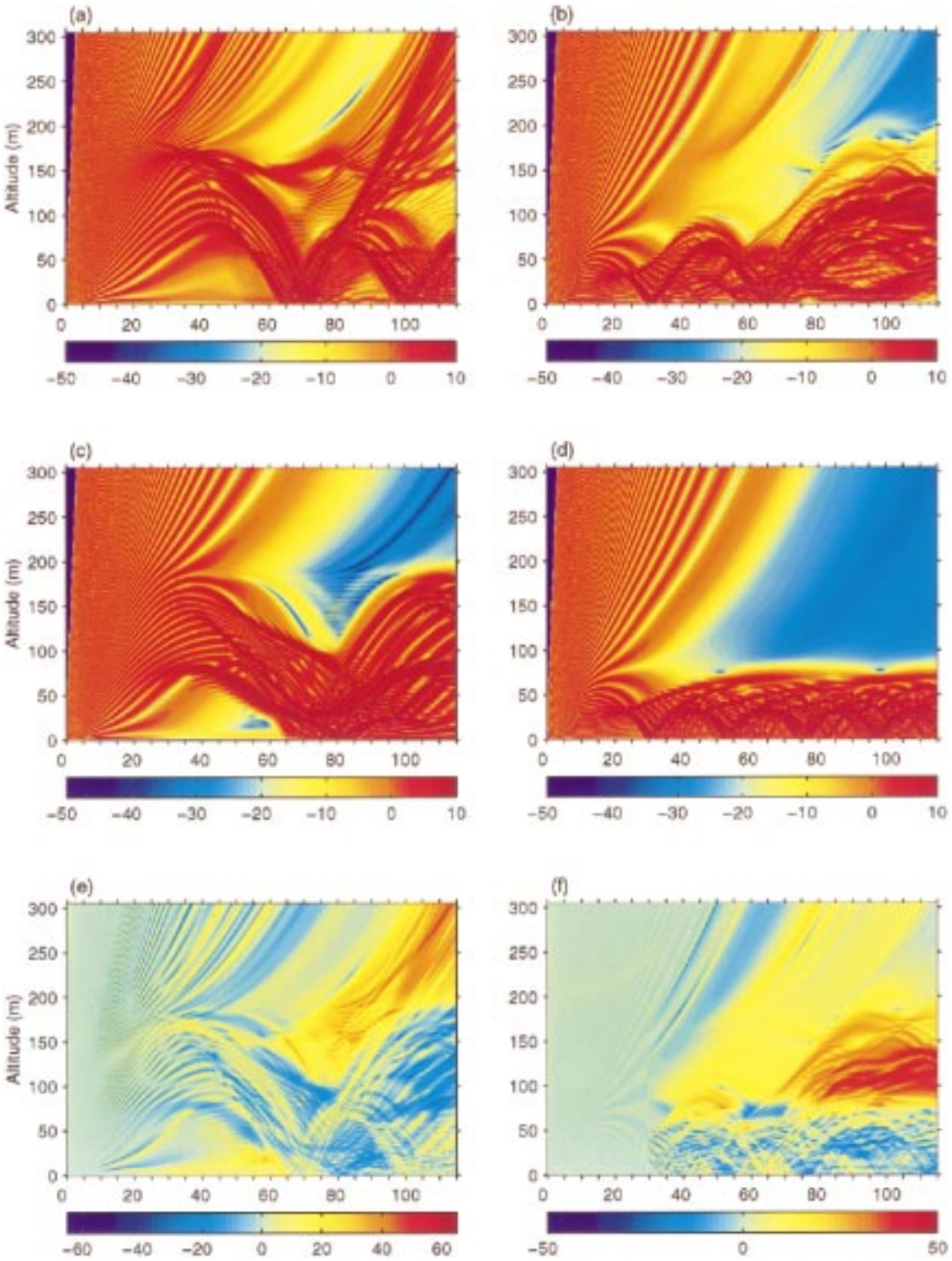

FIG. 19. TEMPER3 model output fields of one-way propagation factor for an X-band radar antenna at 30 m transmitting at 10 GHz: (a) Antenna situated at upwind end of region (left of Fig. 16), all 14 profiles used. (b) Antenna situated at downwind end of region (right of Fig. 16), all 14 profiles used. (c) Antenna situated upwind, single profile collocated with antenna used to define homogeneous conditions. (d) Antenna situated downwind, single profile collocated with antenna used to define homogeneous conditions. (e) Difference between full profile set and single-profile cases for antenna situated upwind [(a)–(c)]. (f) Difference between full profile set and single-profile cases for antenna situated downwind [(b)–(d)]. All altitudes are in meters, horizontal scales are distance from antenna in kilometers, and color scales are in dB.

depth was observed; however, the spatial resolution of the profiles was insufficient to resolve features such as gravity waves directly. Estimates of the wavelength from time series of the vertical velocity during straight and level flight legs within the boundary layer are of the order of 800 m during the low wind cases and up to 4 km during the shamal cases. The continuing evolution of the boundary layer along wind resulted in a general trend in the BL duct structure. The increasing humidity of the boundary layer along wind and consequent increase in the humidity jump across the inversion along wind resulted in an increase in ΔM. In the absence of changes in duct depth this increase would lead to an increase in duct strength. Close to the coast, the IBL and, hence, duct depth will increase rapidly with fetch; when coupled with the increasing humidity, this increase would lead to a rapid increase in the maximum ducted wavelength with distance from the shore. By the time our observations were made, the initial rapid growth of the IBL had slowed or stopped and other processes controlled the duct depth; for example, shear-driven mixing on 25 April led to a reduction in depth and duct strength over the southeastern half of the observation area.

The surface evaporation duct height was estimated using the TOGA COARE bulk parameterization (Fairall et al. 1996) and data from both the C-130 and from deck-mounted instruments on the USS *Caron*. Good agreement was found between the two datasets on all days in spite of concerns that on 23 and 25 April the C-130 observations were made above the nominal surface layer for which the parameterization was developed. The mean duct depth was estimated to be on the order of 10 m on 23 and 25 April and 20–25 m on 27–29 April. Most of the cases had very uniform ducts, with the depth varying by just a few meters over distances of up to 200 km. On 23 April, however, much greater variability, with occasional regions of deeper duct embedded within larger areas of relatively uniform depth, was exhibited. The deeper regions are associated with an increase in the air–sea temperature difference and the consequent change in stability and the shape of the near-surface profiles of temperature, humidity, and refractive index. The onset of mixing across the inversion in the southeastern half of the observation area on 25 April resulted in the deepening of the evaporation duct and an increase in the gradients of heat and humidity across the whole BL with the result that the evaporation duct merged into the BL duct.

Our analysis of the evaporation duct has assumed that the parameterization used is applicable to all the observations. Concerns over the use of measurements taken by the C-130 above the nominal surface layer on 23 and 25 April are allayed somewhat by the close agreement found between the duct heights derived from these observations and those from the ship, made within the surface layer. The change in boundary layer structure observed downwind on 25 April resulted in the evaporation duct merging with the BL duct. The parameterization then found a duct top only well above its range of validity. In the intermediate region between the uniform evaporation duct upwind and the single BL duct downwind, a highly variable and increasing evaporation duct depth was produced by the parameterization. In the absence of simultaneous, collocated measurements of the BL above the surface layer, it is not clear to what extent these values can be trusted or at what point a cutoff must be imposed.

Operational radar propagation models often are used with just a single M profile derived from a bulk parameterization of the surface layer and a sounding of the air above. It is assumed that the duct is sufficiently uniform that the single sounding may be applied to a much wider area. The uniformity of most of the evaporation ducts observed during SHAREM-115 suggests that the assumption of a uniform evaporation duct may be valid for large areas on many occasions. The variability observed on 23 April, however, indicates that there may be situations in which such an assumption could lead to serious errors in the assessment of propagation. Similarly, the rapid change in both evaporation and BL duct structure on 25 April presents a situation where measurements at one end of the observation area would not be applicable at the other.

Comparison of the modeled one-way propagation factors for refractivity structures defined by either a detailed set of profiles or a single profile collocated with the antenna reveal the extent of the errors that may result from the assumption of homogeneity. The results show large contiguous regions with errors considerably in excess of the 5-dB baseline error suggested by Goldhirsh and Dockery (1998). The fractional area of error greater than 5 dB is somewhat greater than that quoted in GD98 from a statistical analysis of 30 cases. The GD98 results are compiled without regard for the actual conditions on the days studied and thus average together cases from a variety of meteorological situations, with and without ducts, with both relatively uniform and highly heterogeneous conditions. Their results indicate that the assumption of homogeneity for a profile collocated with the antenna may lead to significant errors in propagation factor over a 30–90-km range on approximately 40% of occasions, at least for the location where their data were taken. This finding clearly suggests that a single profile frequently will be inadequate to characterize ducting conditions but provides no information as to the conditions for which a single profile may be sufficient. Furthermore, no information is available as to the spatial distribution of the errors, an important consideration in an operational context. A purely statistical approach to the problem of identifying propagation factor errors and defining observational requirements would seem thus to be inadequate.

General trends in BL depth, temperature, humidity, and, hence, duct properties are predictable and thus amenable to modeling. Burk and Thompson (1997) had

some success predicting ducting conditions over the Southern California Bight with a mesoscale model. Trends in trapping layers were predicted with reasonable accuracy by the model; however, it was apparent that large advances were required in data assimilation systems in order to model the *M* field with sufficient fidelity to assess point-to-point propagation losses with any degree of accuracy. The small-scale variability in propagation conditions observed in this study, in particular the effect of the SST on the surface evaporation duct, emphasizes the level of detail that may be required to achieve operationally adequate forecasts of propagation conditions.

In summary, our results have demonstrated the importance of simultaneous measurements of both the surface layer and conditions aloft. Measurements of vertical profiles, for example by radiosonde, are required to characterize the surface-based boundary layer duct that dominated surface propagation conditions throughout SHAREM-115. In the absence of such a strong BL duct, measurements of the surface evaporation duct would be essential to define the near-surface propagation conditions. The results of the propagation modeling study have demonstrated the importance of range-dependent modeling coupled with spatially distributed environmental measurements to characterize accurately radar propagation under heterogeneous conditions. The very dense set of profiles used to define the refractivity conditions in this study is unrealistic for operational use. Further studies are required to identify the minimum environmental sampling requirements under various conditions, and how a limited set of observations can be distributed to maximize their usefulness.

Acknowledgments. This work was supported by the Office of Naval Research Marine Meteorology Program, the U.S. Navy Space and Naval Warfare Command, and the British Meteorological Office. We would like to express our gratitude to the Royal Air Force crew of the C-130 Hercules for their work during this project, and in particular Mr. Chris O'Brien (Officer in Charge) for his help coordinating with the U.S. Navy. We would also like to thank Dr. Michael Newkirk of the Applied Physics Laboratory, the Johns Hopkins University for providing the TEMPER Version 3.0, Beta 6 model code.

REFERENCES

Abdul-Jauwad, S. H., P. Z. Khan, and T. O. Halawani, 1991: Prediction of radar coverage under anomalous propagation conditions for a typical coastal site: A case study. *Radio Sci.,* **26,** 909–919.

Babin, S. M., 1996: Surface duct height distributions for Wallops Island, Virginia, 1985–1994. *J. Appl. Meteor.,* **35,** 86–93.

——, and J. R. Rowland, 1992: Observation of a strong surface radar duct using helicopter acquired fine-scale radio refractivity measurements. *Geophys. Res. Lett.,* **19,** 917–920.

——, G. S. Young, and J. A. Carton, 1997: A new model of the oceanic evaporation duct. *J. Appl. Meteor.,* **36,** 193–204.

Bean, B. B., and E. J. Dutton, 1968: *Radio Meteorology.* Dover Publications, 435 pp.

Burk, S. D., and W. T. Thompson, 1997: Mesoscale modeling of summertime refractive conditions in the Southern California Bight. *J. Appl. Meteor.,* **36,** 22–31.

Craig, R. A., 1946: Measurements of temperature and humidity in the lowest 1000 feet of the atmosphere over Massachusetts Bay. *Pap. Phys. Oceanogr. Meteor.,* **10,** 1–47.

Dockery, G. D., 1988: Modeling electromagnetic wave propagation in the troposphere using the parabolic equation. *IEEE Trans. Antennas Propag.,* **36,** 1464–1470.

Emmons, G., 1947: Vertical distributions of temperature and humidity over the ocean between Nantucket and New Jersey. *Pap. Phys. Oceanogr. Meteor.,* **10,** 1–89.

Fairall, C., E. F. Bradley, D. P. Rogers, J. B. Edson, and G. S. Young, 1996: Bulk parameterization of air–sea fluxes for the Tropical Ocean Global Atmosphere Coupled Ocean–Atmosphere Response Experiment. *J. Geophys. Res.,* **101,** 3747–3764.

Garratt, J. R., 1990: The internal boundary layer—A review. *Bound.-Layer Meteor.,* **50,** 171–203.

——, and B. F. Ryan, 1989: The structure of the stably stratified internal boundary layer in offshore flow over the sea. *Bound.-Layer Meteor.,* **47,** 17–40.

Goldhirsh, J., and D. Dockery, 1998: Propagation factor errors due to the assumption of lateral homogeneity. *Radio Sci.,* **33,** 239–249.

Hsu, S. A., 1983: On the growth of a thermally modified boundary layer by advection of warm air over a cooler sea. *J. Geophys. Res.,* **88** (C1), 771–774.

Moszkowicz, S., G. J. Ciach, and W. F. Krajewski, 1994: Statistical detection of anomalous propagation in radar reflectivity patterns. *J. Atmos. Oceanic Technol.,* **11,** 1026–1034.

Nappo, C. J., and W. D. Bach, 1997: Summary report on the ARO/ARL workshop on turbulence and diffusion in the stable planetary boundary layer. *Bull. Amer. Meteor. Soc.,* **78,** 493–498.

Perrone, T. J., 1979: Winter Shamal in the Persian Gulf. Naval Environmental Publ. Research Facility, Monterey, CA, Rep. NEPRF-TR-7906, 180 pp. [Available from NRL-Monterey, 7 Grace Hopper Avenue, Monterey, CA 93943.]

Rogers, D. P., D. W. Johnson, and C. A. Friehe, 1995: The stable internal boundary layer over a coastal sea. Part I: Airborne measurements of the mean and turbulence structure. *J. Atmos. Sci.,* **52,** 667–683.

Sandwell, D. T., 1987: Biharmonic Spline Interpolation of GEOS-3 and SEASAT Altimeter Data. *Geophys. Res. Lett.,* **14,** 139–142.

Smedman, A.-S., H. Bergström, and B. Grisogono, 1997: Evolution of stable internal boundary layers over a cold sea. *J. Geophys. Res.,* **102** (C1), 1091–1099.

Stull, R., 1988: *Boundary Layer Meteorology.* Kluwer Academic, 666 pp.

Turton, J. D., D. A. Bennetts, and S. F. G. Farmer, 1988: An introduction to radio ducting. *Meteor. Mag.,* **117,** 245–254.